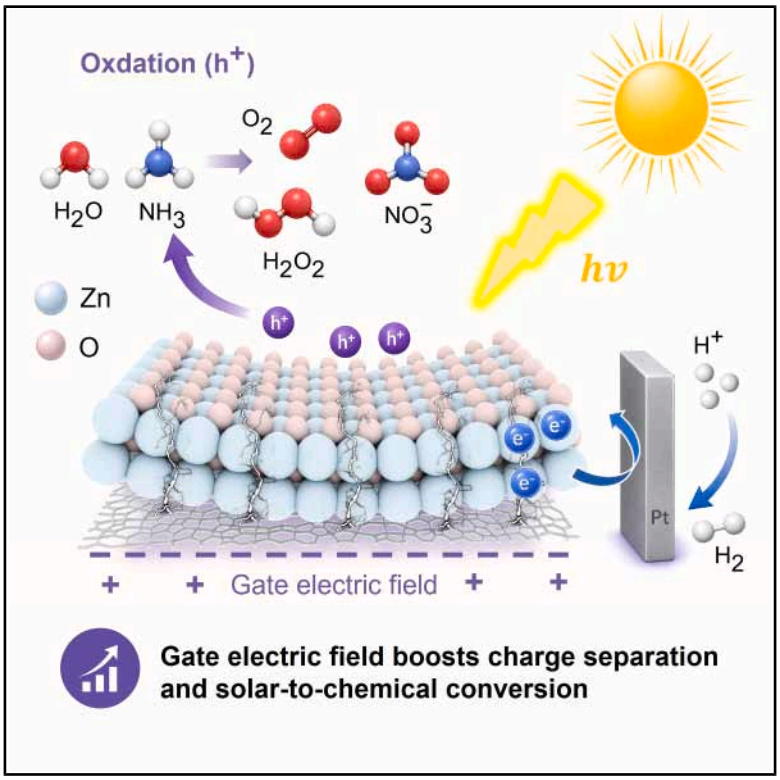
Device

Article

Electrostatic field-driven photocarrier separation in ZnO photoanodes for enhanced photoelectrochemical efficiency

Graphical abstract



Authors

Xinkong Wei (魏鑫孔), Tianhao He (何天浩), Yu Xie (谢瑜), Yue Pei (裴悦), Xiang Li (李想), Weihua Han (韩卫华), Di Wei (魏迪)

Correspondence

hanwh@lzu.edu.cn (W.H.), weidi@binn.cas.cn (D.W.)

In brief

Wei et al. demonstrate transistor-inspired gate control of carrier dynamics in photoelectrochemical electrodes. Their vertical field-effect photoanode drives gate electric field penetration through ZnO, modulating band bending, guiding carrier transport, and suppressing recombination to enhance photogenerated charge separation and interfacial charge transfer.

Highlights

- A vertical field-effect photoanode uses gate bias to regulate photoanode performance
- The gate field penetrates the ZnO layer, driving carrier separation and transport
- Gate-induced band bending and carrier-channel formation at the nanoscale
- The low-energy field effect enhances PEC performance in multiple metal-oxide photoanodes

Explore
Early prototypes with exciting performance and new methodology

Wei et al., 2026, Device *4*, 101185
August 21, 2026 © 2026 Elsevier Inc. All rights are reserved, including those for text and data mining, AI training, and similar technologies.
https://doi.org/10.1016/j.device.2026.101185

CellPress

Device

CellPress

Article

Electrostatic field-driven photocarrier separation in ZnO photoanodes for enhanced photoelectrochemical efficiency

Xinkong Wei (魏鑫孔),[1] Tianhao He (何天浩),[1] Yu Xie (谢瑜),[1] Yue Pei (裴悦),[1] Xiang Li (李想),[2] Weihua Han (韩卫华),[1,*] and Di Wei (魏迪)[2,3,4,*]

[1]School of Physical Science and Technology, Lanzhou University, Lanzhou 730000, P.R. China
[2]Beijing Institute of Nanoenergy and Nanosystems, Chinese Academy of Sciences, Beijing 101400, P.R. China
[3]Centre for Photonic Devices and Sensors, University of Cambridge, 9 JJ Thomson Avenue, CB3 0FA Cambridge, UK
[4]Lead contact
*Correspondence: hanwh@lzu.edu.cn (W.H.), weidi@binn.cas.cn (D.W.)
https://doi.org/10.1016/j.device.2026.101185

THE BIGGER PICTURE A challenge in solar-driven chemical conversion is that light generates positive and negative charges inside a semiconductor, but many of these charges disappear before they can drive useful reactions at the surface. Researchers try to solve this problem by changing the material composition, adding junctions, or depositing catalytic layers. These approaches can improve performance, but they may introduce defects, complicate fabrication, and reduce stability. Another difficulty is that charge motion occurs inside the active layer, where it is hard to control during operation. Here, we address this challenge using a vertical field-effect photoanode, in which an external electrostatic gate field guides charge movement across ZnO. This electrical control modulates band bending via the gate-induced electrostatic field, separating photogenerated charges and improving charge transport without relying on permanent chemical or structural modification of the semiconductor.

SUMMARY

Photoelectrochemical (PEC) performance is limited by the efficiency of photocarrier separation and bulk recombination in metal-oxide photoelectrodes. Here, we develop a vertical field-effect photoanode (VFEPA) by integrating a field-effect transistor architecture into a ZnO photoanode. The gate-tunable electric field dynamically regulates band bending and carrier transport across the photoactive layer, promoting electron-hole separation and enhancing interfacial charge transfer. As a result, the photocurrent density increases from 0.35 to 0.85 mA cm^{-2} at 1.2 V vs. reversible hydrogen electrode (RHE), while the incident photon-to-current efficiency (IPCE) improves from 4.2% to 17.5% under a 6 V gate bias with negligible energy cost. Spatially resolved Kelvin probe force microscopy and surface photovoltage mapping reveal gate-induced electrostatic redistribution and enhanced directional charge transfer. This vertical field-effect strategy is applicable to metal-oxide photoelectrodes for electrostatic control of carrier dynamics in PEC systems.

INTRODUCTION

The overall efficiency of photoelectrochemical (PEC) systems is governed by the properties of the photoelectrode, which is responsible for light absorption, photocarrier generation, and the provision of active reaction sites.[1] Metal-oxide semiconductors are used in PEC applications due to their chemical stability, Earth abundance, and low fabrication cost.[2,3] Nevertheless, their practical PEC performance remains below the requirements for industrial deployment. This gap originates from bulk and interfacial carrier recombination,[4] intrinsically low carrier mobility,[5] and limited solar spectral utilization,[6] collectively constraining achievable solar-to-fuel conversion efficiencies.[7] Among these limitations, inefficient photocarrier separation and collection within the photoelectrode bulk represent a critical bottleneck.[8–10] Experimental studies indicate that typically only ~10% of photocarriers reach the semiconductor-electrolyte interface to participate in surface redox reactions.[11,12] These strategies can suppress the recombination and promote directional carrier transport throughout the entire photoelectrode thickness, rather than at interfaces, and are essential for advancing PEC performance.[13]

All rights are reserved, including those for text and data mining, AI training, and similar technologies.

Internal electric fields are recognized as a driving force for charge separation and transport, and their incorporation into photoelectrodes offers a pathway to mitigate bulk recombination losses.[14–16] Routes to introduce such fields include surface passivation,[17–19] heterojunction construction,[20–23] and gradient homojunction engineering.[24–26] While these strategies can generate interfacial electric fields that assist carrier separation, they often entail intrinsic trade-offs: band misalignment and large energetic offsets restrict material selection and may limit attainable photovoltage,[27–30] whereas heterointerfaces can introduce structural defects that act as recombination centers and compromise catalytic activity. Gradient homojunctions alleviate some interfacial penalties but remain challenging because they require stringent compositional control and material compatibility.[31,32]

Beyond static interfacial band engineering, field sources such as piezoelectric/ferroelectric/pyroelectric polarization have been explored to manipulate band bending and carrier distribution in PEC systems.[33–38] Representative advances include piezo-assisted ZnO photoanodes under ultrasonic excitation to strengthen internal fields and the coupling of ZnO/Cu_2O heterojunctions with Co Pi cocatalysts to simultaneously broaden absorption and accelerate interfacial hole transfer.[39] In parallel, phase-boundary and defect engineering in piezoelectric oxides has been used to amplify polarization fields and promote directional charge migration. For example, Ca^{2+}-modified $BaTiO_3$ with tetragonal orthorhombic phase coexistence and Ti^{3+}-related shallow states can enhance internal polarization and facilitate charge separation.[40] Surface modification via ion embedding has also been shown to enhance polarization and suppress recombination, exemplified by Cl^--embedded $BiVO_4$, in which polar-group distortion modifies the oxygen evolution pathway and facilitates hole access to active sites.[41] These developments, together with recent reviews on ZnO-based photoanode modulation strategies, underscore the broad interest in leveraging polarization-driven fields for carrier regulation.[42] Despite their appeal, polarization- or stimulus-enabled fields are limited by constrained field strength and directionality, dependence on external mechanical/thermal stimuli, and susceptibility to defect- or interface-mediated recombination and stability issues, often resulting in performance that is sensitive to operating conditions. These limitations motivate different field-regulation strategies capable of delivering strong, continuously tunable, and spatially controllable electric fields without introducing additional recombination pathways while remaining compatible with established photoelectrode optimization schemes.

Integrating field-effect transistors (FETs) with optoelectronic devices can help regulate carrier density and transport.[43–46] Field-effect modulation has proven transformative in organic light-emitting diodes (OLEDs) and thermoelectric systems, where it enables dynamic control over charge transport and device efficiency.[47,48] FET-based field regulation could offer a route to overcome carrier management limitations in PEC photoelectrodes.

In this study, we fabricate an integrated gate-controlled ZnO photoanode device, termed a vertical field-effect photoanode (VFEPA). The device integrates a conductive Si gate, an SiO_2 dielectric layer, a ZnO photoactive layer, and an Al network current collector, enabling an external gate bias to generate a vertical electrostatic field across the ZnO photoactive layer during PEC operation, thereby modulating band bending, carrier transport, and charge separation. ZnO was chosen as a model system because its semiconductor properties and interfacial energetics are well understood, making it suitable for clarifying the effects of gate-induced band modulation on photocarrier dynamics. Other strategies, such as doping, heterojunction engineering, and cocatalyst loading, optimize interfacial energetics or reaction kinetics, but they offer limited and largely non-reversible control over bulk carrier transport and can introduce additional defect-mediated recombination pathways. In contrast, the gate electrostatic field offers a reversible and continuously tunable physical route to regulate the internal electric field across the active layer. As a result, photocarrier separation and directional transport are enhanced, while bulk recombination is suppressed. Kelvin probe force microscopy (KPFM) and surface photovoltage (SPV) mapping further confirm the gate-induced modulation of band bending and interfacial charge separation. This work establishes a broadly applicable field-regulation concept for designing efficient and controllable PEC devices.

RESULTS AND DISCUSSION

Design and working principles of the ZnO-based VFEPA

To address the challenge of inefficient carrier separation and recombination in conventional PEC photoanodes, we develop a field-effect-regulated photoanode guided by the principle of spatially resolved electric-field engineering. By introducing a vertical gate field into the photoanode architecture, this design enables active modulation of photocarrier dynamics, overcoming intrinsic limitations in charge transport and collection. As shown in Figures 1A and 1B, the VFEPA integrates a ZnO active layer with a bottom-gate VFET configuration, enabling vertical carrier transport. The heavily doped p-type silicon substrate serves as the gate terminal due to its high electrical conductivity (Figures 1A and S1), while the native SiO_2 layer functions as a dielectric barrier, isolating the gate from the source to prevent charge leakage and neutralization. A crack-patterned Al nanomesh, deposited atop the dielectric, serves as the source terminal. This mesh facilitates efficient electron collection from the active layer and minimizes the shielding of the gate-induced electric field, achieving an optimized balance between conductivity and field penetration. Subsequently, a ZnO active layer is deposited as the photoactive layer, and the overlying electrolyte functions analogously to the drain terminal, extracting photogenerated holes under the influence of the vertical gate field. The complete fabrication process is illustrated in Figure S2. The working mechanism of the VFEPA is illustrated in Figure 1B–1E. When a positive gate voltage is applied, the resulting electric field penetrates the dielectric layer and extends into the ZnO/Al interface region through the porous electrode (Figure 1C). The applied gate field in the vertical field-effect architecture reshapes the carrier vertical transport channel, similar to gate modulation in conventional FETs. By strengthening the vertical electric field within the ZnO layer, the gate bias redistributes the internal potential landscape, preferentially driving electrons toward the Al

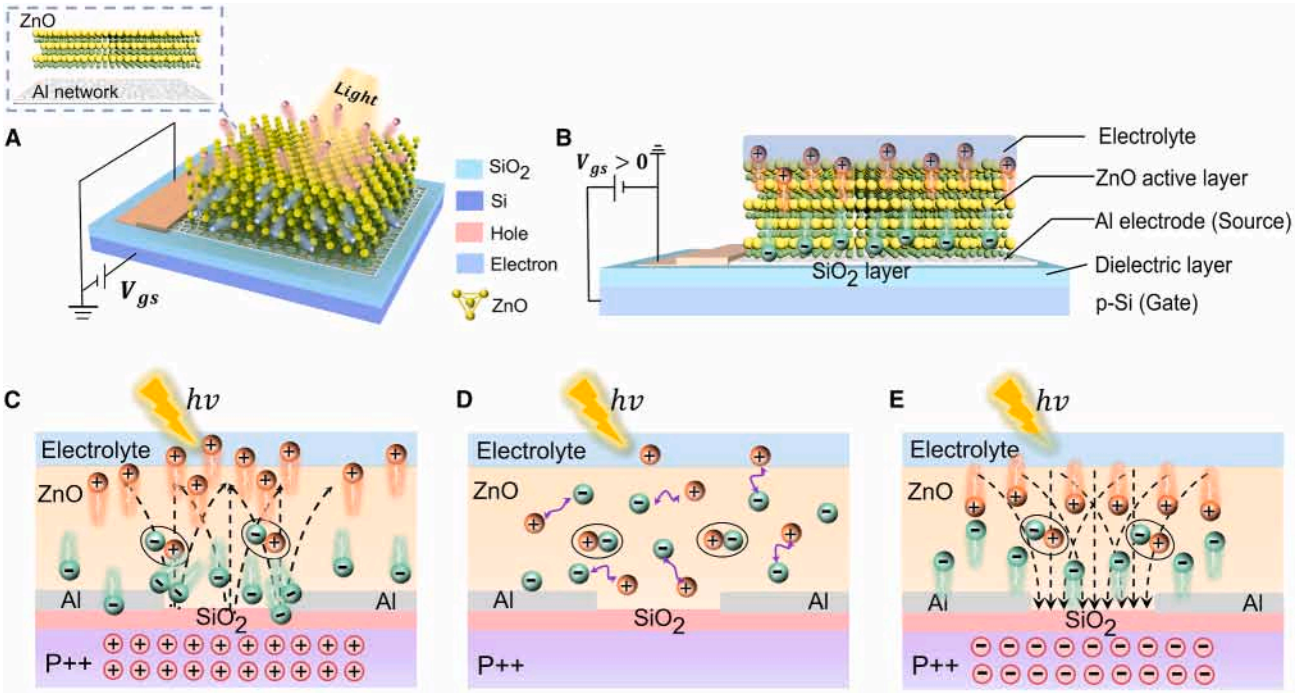


Figure 1. Design principle and working mechanism of the VFEPA

(A and B) Device structure of the photoanode with vertical field effect and a schematic diagram of photocarrier migration under the vertical gate electric field. (C–E) Schematic diagrams of the corresponding carrier distributions and migration pathways under positive, zero, and negative gate bias conditions.

electrode for efficient extraction while facilitating hole migration toward the ZnO/electrolyte interface for oxidation reactions. This field-induced channel regulation promotes directional charge transfer and suppresses interfacial recombination, enhancing the overall PEC activity. Figures 1C–1E compare carrier dynamics under different gate bias conditions. Positive gate bias opens the vertical transport channel: it lowers the ZnO/Al barrier for electron extraction and strengthens band bending at the ZnO/electrolyte side, driving holes to the surface; thus, carrier separation and transport are strongly enhanced. Without gate bias, no vertical transport channel forms, carriers move randomly, recombination dominates, and extraction remains limited. Negative bias reverses the field, raising the ZnO/Al barrier and weakening the depletion region at the electrolyte side. Electrons pile up at the surface while holes are blocked. Equivalently, the vertical transport channel is "pinched off," suppressing both separation and transport, aggravating recombination, and reducing PEC activity.

Structural and material characterization of the VFEPA

Figure 2 presents comprehensive structural and optical characterizations of the VFEPA, confirming the fabrication of the designed multilayer architecture and the integrity of its functional components. Atomic force microscopy (AFM) and SEM analyses (Figures 2A and S3) show that the ZnO active layer consists of uniformly sized, densely packed nanograins with clear boundaries. Statistical data (Figure S4) indicate an average grain diameter of ~53 nm and height of ~11 nm. The low roughness and compact structure enhance light absorption and increase surface reaction sites. Cross-sectional SEM (inset of Figure 2A) confirms a uniform multilayer structure with ZnO and SiO_2 layers ~400 and ~300 nm thick, respectively. This architecture ensures strong gate-channel coupling, enabling efficient field modulation and charge transport. Figure 2B presents a SEM image of the VFEPA device, in which the ZnO active layer is conformally deposited on a uniformly distributed Al mesh electrode. This electrode architecture minimizes gate-field shielding and enables gate electric field penetration, while its high electrical conductivity ensures efficient collection of photogenerated electrons (Figure S5). The Al mesh features an average line width of ~4 μm and a height of ~250 nm (Figure S6) and is integrated atop a SiO_2 dielectric layer and a heavily doped p++ Si substrate—consistent with the vertical structure outlined in Figure 1. The mesh is well connected and evenly spaced, with its areal density readily tunable by adjusting the spin-coating speed, offering a means to balance gate-field distribution and photogenerated electron collection efficiency (Figure S7). The ZnO active layer deposited on bare SiO_2 and Al mesh/SiO_2 substrates exhibits comparable surface roughness values (0.78 and 0.80, respectively; Figure S8), indicating that the underlying Al mesh electrode has a negligible impact on the morphological integrity of the ZnO active layer. Figure 2C shows the energy-dispersive X-ray spectroscopy (EDS) elemental mapping of the VFEPA device, confirming the construction of the designed multilayer architecture. Zn and O signals are uniformly distributed in the upper region, corresponding to the ZnO layer. The Al signal outlines a continuous mesh structure beneath ZnO, while the Si and O signals indicate the underlying SiO_2/p++Si substrate. The

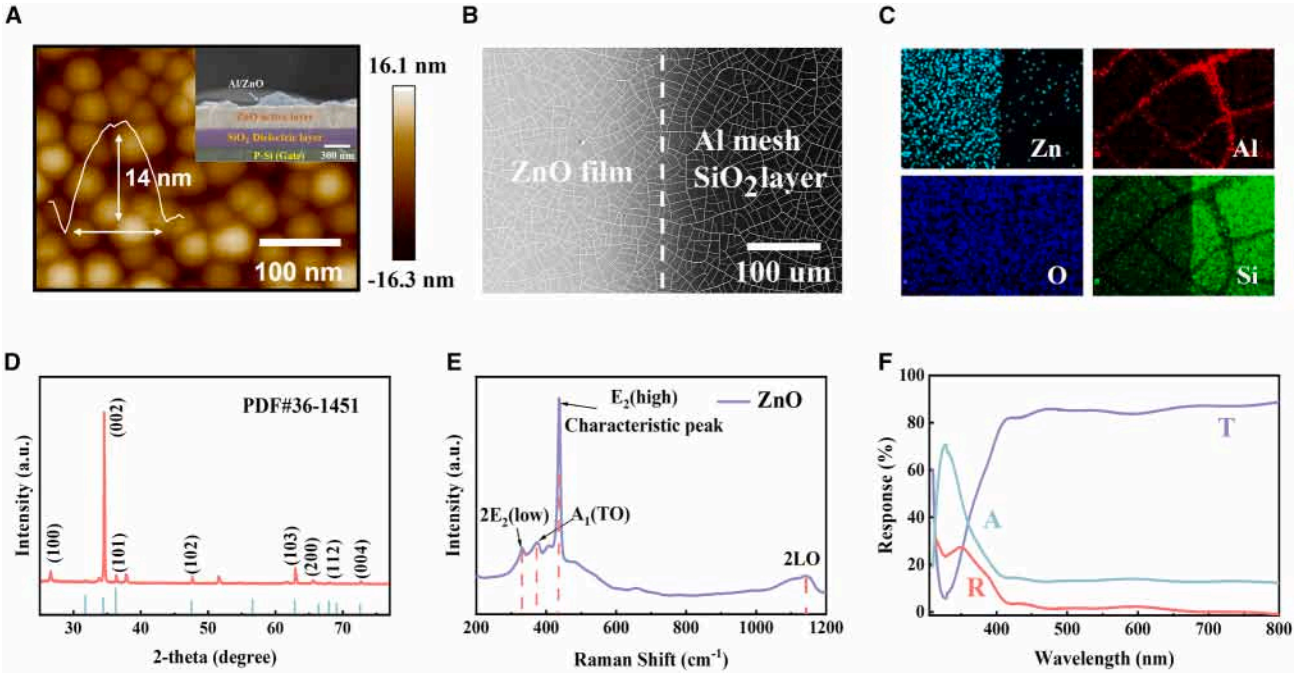


Figure 2. Morphological and structural characterization of the VFEPA

(A) Atomic force microscopy (AFM) image of the ZnO active layer; inset shows the cross-sectional scanning electron microscopy (SEM) image of the VFEPA (scale bars: 100 nm in the AFM image and 300 nm in the cross-sectional inset).

(B and C) Plan-view SEM image and corresponding energy-dispersive spectroscopy (EDS) mapping of the VFEPA (scale bars: 100 μm in the SEM image).

(D) X-ray diffraction (XRD) pattern of the ZnO active layer.

(E) Raman spectrum of the ZnO active layer.

(F) UV-vis absorption spectra (A, absorbance; T, transmittance; R, reflectance) of the ZnO active layer.

distinct spatial distribution of each element verifies that the fabricated structure matches the intended device configuration. The crystallinity and crystal phase of the ZnO were investigated using X-ray diffraction (XRD) patterns (Figure 2D). The results show that the film has a high-purity hexagonal wurtzite structure, with all diffraction peaks matching well with standard hexagonal ZnO (JCPDS 36-1451). To clarify the local microstructure of the ZnO active layer, transmission electron microscopy (TEM) and high-resolution TEM (HRTEM) characterizations were performed (Figure S9). The TEM image reveals the granular morphology of the ZnO film, while the HRTEM images display clear lattice fringes with interplanar spacings of 0.24 and 0.19 nm, corresponding to the ZnO (101) and (102) planes, respectively. These results are consistent with the XRD analysis and confirm the crystalline wurtzite structure of the ZnO active layer. In addition, high-angle annular dark-field (HAADF) imaging combined with EDS elemental mapping shows a uniform distribution of Zn and O, verifying the compositional homogeneity of the ZnO film. The Raman spectrum (Figure 2E) of the ZnO active layer exhibits characteristic peaks at approximately 332, 381, 438, and 1,157 cm^{-1}, corresponding to the $2E_2$ (low), A_1(TO), E_2 (high), and 2LO modes of ZnO, respectively, indicating a typical hexagonal wurtzite structure. In particular, the strong E_2 (high) peak suggests high crystalline quality.[49,50] X-ray photoelectron spectroscopy (XPS) spectra confirm the presence of Zn, O, Al, and Si, consistent with the device composition (Figure S10). The Zn 2p peak indicates Zn^{2+} states, while the O 1s signal contains contributions from lattice oxygen and surface oxygen vacancies, O^{2-} ions in Zn–O bonds within the ZnO lattice, confirming the presence of crystalline ZnO. Al 2p and Si 2p peaks correspond to the mesh electrode and substrate, respectively. These results demonstrate the successful fabrication of the designed VFEPA structure with well-defined component distribution. Optical properties of the ZnO active layer were evaluated by UV-visible (UV-vis) spectroscopy (Figure 2F). A sharp absorption edge at ~400 nm indicates strong UV absorption and limited visible-light absorption, which helps suppress recombination under solar illumination. In the 400–800 nm range, the film exhibits high transmittance, exceeding 80% above 600 nm, indicating excellent optical transparency.

Field effect on carrier distribution in the VFEPA

To clarify the mechanism of gate-induced modulation, we simulated the photocarrier distribution and band structure evolution in the VFEPA device. Figures 3A and 3B show the simulated electric field distribution in the VFEPA under a gate bias of Vgs = 6 V. The gate field penetrates through the dielectric and ZnO active layer, with enhanced intensity in the void regions between the Al mesh electrode due to reduced shielding. A clear vertical potential gradient is established within the ZnO active layer, providing a strong driving force for carrier separation. This field drives electrons downward toward the source terminal

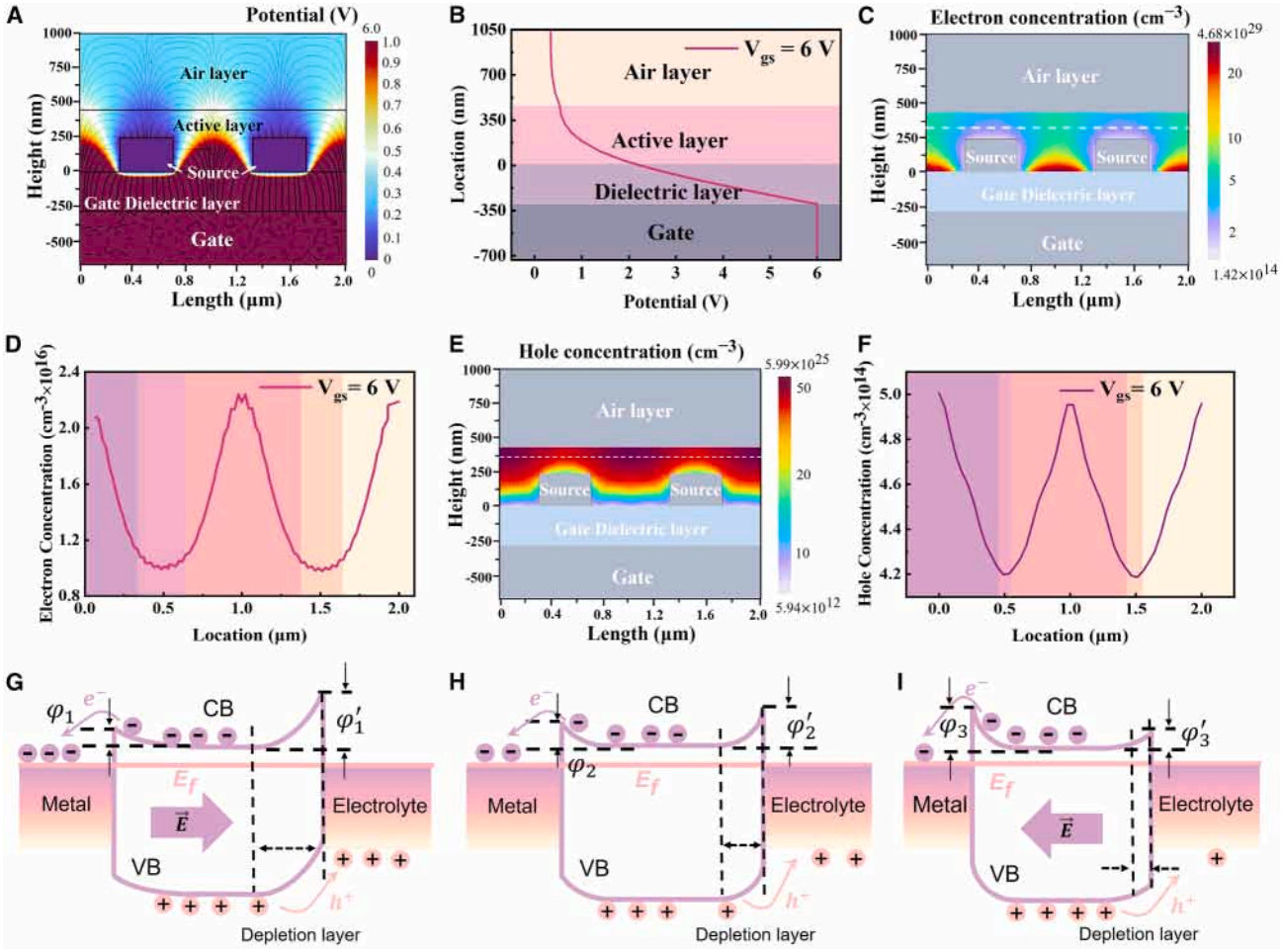


Figure 3. Gate-tunable electrostatic regulation of carrier distribution and band energetics in the VFEPA architecture

(A) Theoretical simulation of electric potential distribution at Vgs = 6 V.

(B) Simulated electrostatic potential profile along the vertical axis of the device.

(C and D) Theoretical simulation of electron density distribution at Vgs = 6 V.

(E and F) Corresponding theoretical simulation of hole density distribution at Vgs = 6 V, with holes migrating toward the ZnO/air layer interface.

(G–I) Energy band diagrams of the VFEP under positive, zero, and negative gate bias, respectively.

and holes upward toward the electrolyte, supporting efficient photocarrier extraction and validating the vertical field-effect modulation concept. Figure 3C and 3D show the electron distribution inside the device under positive gate bias and illumination. The Al mesh screens the gate potential beneath the metal, so the vertical gate field primarily penetrates through the mesh void regions, lowering the local conduction band edge and forming vertical transport channels with high electron density beneath the void regions. Electrons migrate downward along these channels and then laterally toward the mesh for collection, analogous to the gate-controlled channels in FETs that periodically recur with the mesh pitch, suppressing interfacial recombination and enhancing carrier-separation efficiency.

Similarly, Figures 3E and 3F show the simulated hole distribution. Holes tend to accumulate near the top surface of the ZnO active layer, particularly in the mesh void regions, indicating that the gate field effectively penetrates the unshielded areas and drives upward hole migration. The hole concentration also exhibits a periodic lateral variation, with higher density in the voids and lower density beneath the metal. This distribution reflects field-guided vertical transport, enhancing hole injection at the ZnO/electrolyte interface and enabling spatially selective charge separation. The field-penetration-induced carrier redistribution is directly consistent with the spatially resolved measurements (Figure 4): in the KPFM/SPV analysis, both the surface potential (V_{CPD}) and the SPV signal over the void regions increase monotonically with gate bias, indicating surface hole accumulation and dynamically modulated interfacial band bending; meanwhile, the local photocurrent maps show a stronger response in the same void regions, reflecting enhanced photocarrier transport and the formation of an effective conductive pathway.

At zero gate bias (Figure 3H), the ZnO/electrolyte interface exhibits conventional upward band bending, determined by

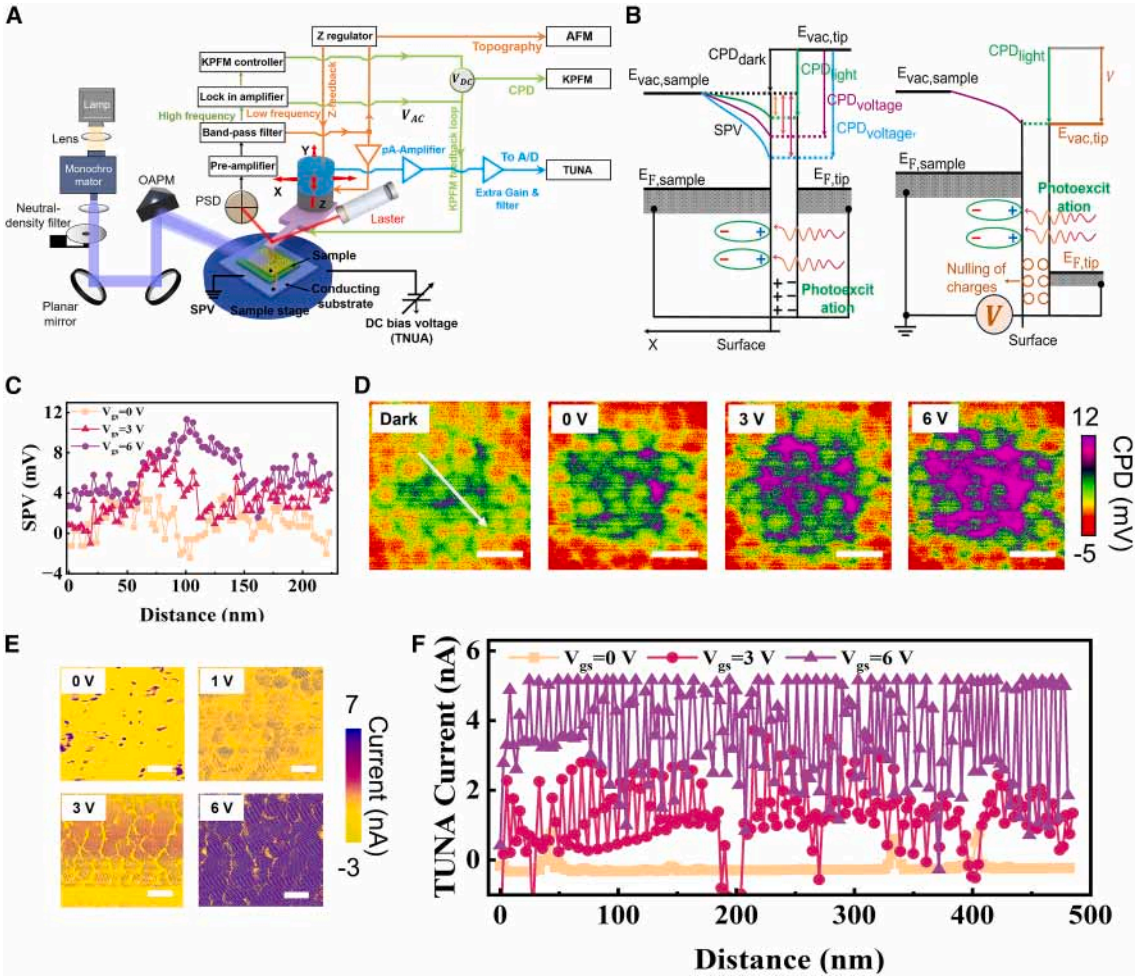


Figure 4. Gate-voltage-controlled surface potential and carrier transport mechanisms

(A) Schematic diagram of the setup for measuring electrical properties based on the photoconductive module.

(B) Schematic illustration of the principle for measuring the SPV signal of the sample using the photoconductive module.

(C) Line profiles of SPV signal extracted along the white arrows in (D), acquired entirely within the mesh void regions to probe gate-field penetration.

(D) Representative V_{CPD} map of the device surface under different gate voltages, showing a monotonic increase in surface potential within the void regions (scale bars: 100 nm in the KPFM image).

(E and F) Tunneling atomic force microscopy (TUNA) photocurrent maps measured on the device surface under different gate voltages (scale bars: 100 nm in the TUNA photocurrent maps).

Fermi-level alignment, resulting in a relatively wide depletion region that enables basic charge separation but provides only a limited driving force for interfacial reactions. The Al/ZnO contact sustains a finite Schottky barrier accompanied by a depletion layer, which constrains electron extraction. In the absence of gate-induced conduction channels, carrier transport occurs primarily via diffusion and the built-in electric field, leading to enhanced recombination and reduced overall charge-separation efficiency.

At positive gate bias (Figure 3G), the ZnO/electrolyte interface undergoes reinforced upward band bending, which broadens the depletion region and strengthens the driving force for hole transfer toward the electrolyte while repelling electrons away from the surface. This enhanced separation lowers the probability of interfacial recombination. Simultaneously, beneath the void regions of the Al mesh, the penetrating gate field lowers the conduction band edge, creating vertically confined high-density electron channels. At the Al/ZnO interface, the effective Schottky barrier is reduced, and the depletion layer narrows, facilitating efficient electron injection into the metallic mesh. These effects resemble the channel opening in a FET, where the gate field defines conductive pathways, improving charge separation and photocurrent output.

At negative gate bias (Figure 3I), the band alignment at the ZnO/electrolyte interface is distorted in the opposite direction, resulting in weakened upward bending or even downward band bending. This compression of the depletion region promotes electron accumulation near the surface while displacing photogenerated holes away from the interface, severely hampering interfacial hole transfer and enhancing recombination. At the

Al/ZnO contact, the Schottky barrier height increases and the depletion width expands, raising the energetic barrier for electron injection into the metallic mesh. In transistor terminology, this situation corresponds to channel pinch off, where the gate field suppresses carrier transport and degrades photocurrent performance.

Spatial mapping of gate-driven charge separation

The photoconductive characterization platform was employed to investigate surface-charge behavior and carrier transport in the VFEPA device under different gate voltages. Figures S11 and S12 show the AFM and electrostatic AFM (EFM) results of the p-type Si/SiO_2/Al mesh electrode structure. At Vgs = 0 V, a weak electrostatic interaction is observed on the SiO_2 surface, indicating limited gate-field influence. As the gate voltage increases to 1 and 3 V, the electrostatic force above the SiO_2 region strengthens, while it remains weak in Al-covered areas due to shielding. This confirms that the gate field selectively penetrates through the mesh voids to modulate the ZnO active layer beneath.

To investigate carrier behavior, a multimodal AFM photoconductive characterization platform was used (Figure 4A), integrating photoexcitation with KPFM, tunneling AFM (TUNA), and topographic AFM. A xenon arc lamp coupled with a monochromator delivers tunable monochromatic light (300–800 nm, 1–10 mW/cm^2) to induce SPV signals. KPFM measures surface potential and SPV signals, and TUNA provides localized photocurrent mapping by applying a bias voltage under photoexcitation, while AFM captures surface morphology to correlate topographic features with charge transport behavior. This system enables spatially resolved analysis of gate-field effects on photocarrier dynamics. The working principle of SPV measurement is shown in Figure 4B. The V_{CPD} between the sample and probe reflects surface band bending and varies with carrier redistribution under illumination. Photogenerated holes migrate toward the surface, increasing the V_{CPD} and yielding a positive SPV signal, defined as

$$SPV = V_{CPD-light} - V_{CPD-dark} \quad \text{(Equation 1)}$$

Conversely, electron accumulation at the surface reduces V_{CPD}, resulting in a negative SPV signal. The magnitude and sign of the SPV signal provide direct insights into the type and direction of carrier separation. Figures S13 and 4C show the line profiles of V_{CPD} and SPV signals extracted along the white arrows indicated in Figure 4D. In the dark, V_{CPD} remains low and stable, consistent with the absence of charge separation. Upon illumination, V_{CPD} rises markedly, confirming the migration of photogenerated holes toward the ZnO surface. As gate voltage increases, the average V_{CPD} increases, demonstrating that the gate-induced electric field effectively penetrates the active layer and enhances vertical carrier separation. This trend is corroborated by the SPV signal, which also grows with gate bias. Stronger SPV signals indicate more efficient electron-hole separation and suppressed recombination, while the positive SPV polarity confirms hole accumulation at the surface and electron transfer into the source terminal. This gate-dependent SPV response is in good agreement with the carrier-migration simulations in Figure 3, which predict upward hole drift toward the ZnO/electrolyte interface and downward electron transport into the mesh-defined channels under positive gate bias.

The surface potential maps in Figures 4D and S14 provide further evidence: as the gate voltage increases, the potential rises and is more uniformly distributed across the void regions, indicating deeper field penetration, the formation of a stable hole-accumulation region, and more efficient carrier extraction with suppressed recombination. These results highlight the central role of gate modulation in optimizing charge transport dynamics. Figures 4E, 4F, and S15 display TUNA photocurrent maps under different biases. At Vgs = 0 V, the current is negligible, indicating poor conductivity. As the gate bias increases, the photocurrent density becomes stronger and more uniform, with clear grain boundary contrast—suggesting improved carrier mobility and the formation of effective conductive channels. Together, the consistent trends observed in V_{CPD}, SPV, and TUNA photocurrent measurements provide strong experimental support for the simulated field-driven carrier behavior. Gate bias not only enhances photocarrier separation but also improves charge extraction and transport, which are essential for optimizing PEC device performance.

Gate-controlled PEC response of ZnO-based VFEPA devices

Gate-voltage modulation of PEC performance in the VFEPA device was systematically evaluated, as shown in Figure 5. PEC measurements were performed using a three-electrode probe system (Figure 5A), where the electrolyte was dropped onto the surface of the VFEPA, with the working electrode (WE) connected to the Pt probe and in contact with the source terminal. The platinum (Pt) wire electrode served as the counter electrode (CE) and was inserted into the electrolyte, and Ag/AgCl served as the reference electrode (RE). The current density between the device and the Pt electrode was measured under varying gate voltages. A photograph of the experimental setup used during the PEC measurements is provided in Figure S16.

Figures 5B (with a sacrificial agent) and 5C (without a sacrificial agent) show the current density-voltage (J-V) curves of the VFEPA under different gate voltages. With increasing Vgs, the photocurrent density increases steadily, reaching a maximum of 0.85 mA cm^{-2} at Vgs = 7 V, which is 2.4 times that at zero bias, and then gradually approaches saturation at higher gate voltages. The thickness-dependent PEC performance and benchmark comparison with representative ZnO-based photoelectrodes are discussed in Note S2, Figures S17–S19, and Table S1.

Figure 5D displays the real-time photocurrent response under stepwise gate voltages during periodic light-on/light-off cycles. At Vgs = 0 V, the device shows a moderate photocurrent response that progressively increases as gate voltage rises. This trend demonstrates enhanced carrier-separation and transport efficiency induced by the applied gate electric field. Simultaneously, reproducible on/off switching behavior across all voltage steps confirms the device's excellent photoresponse stability and gate-tunable PEC performance. The long-term operational stability of the VFEPA was evaluated under continuous illumination (Figure S20). The photocurrent remains stable for 1,800 s at both Vgs = 0 V and Vgs = +6 V without noticeable decay. Notably, the device maintains a consistently higher photocurrent under gate bias throughout the test, indicating

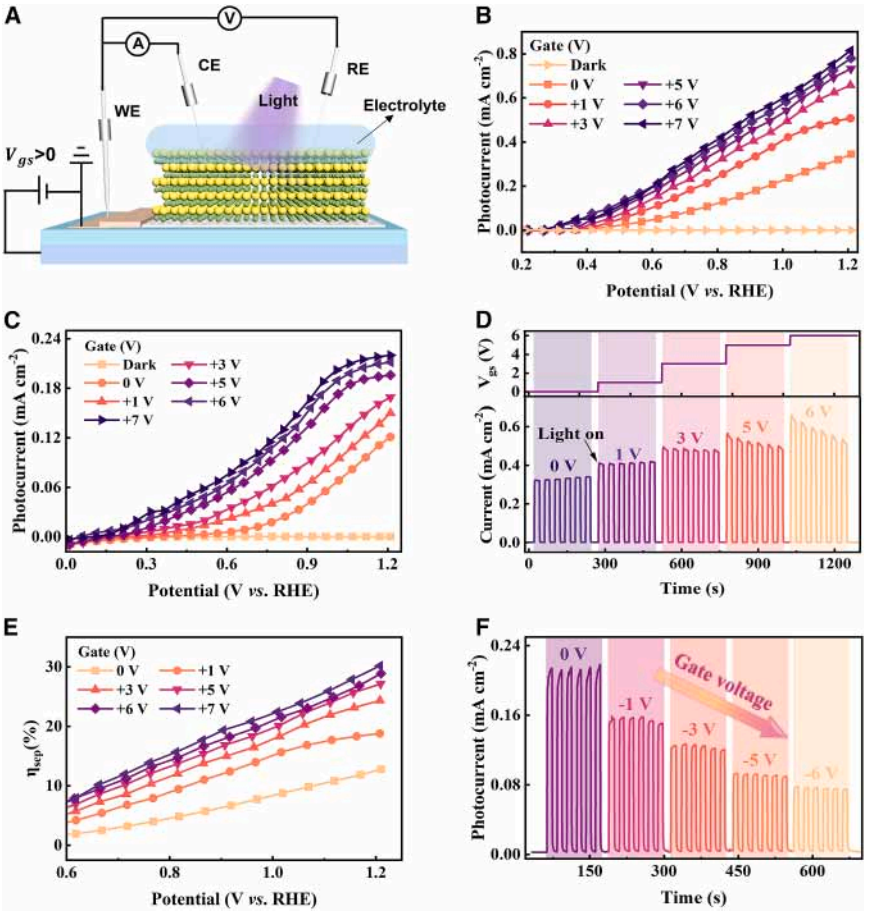


Figure 5. PEC performance of VFEPA under different gate voltages

(A) Schematic of PEC testing using a three-electrode probe system.

(B) J-V response of the VFEPA under different gate voltages with 0.1 M Na_2SO_3 as a hole scavenger.

(C) J-V curves of the VFEPA measured under different gate voltages in the absence of a sacrificial agent.

(D) Light-chopping response under different gate voltages (with hole scavenger, polarization potential = 0.4 V vs. Ag/AgCl).

(E) Charge-separation efficiency (the theoretical maximum photocurrent density of the ZnO photoanode is 2.57 mA cm^{-2}).

(F) Light-chopping response under reverse gate bias conditions (with hole scavenger, polarization potential = 0.3 V vs. Ag/AgCl).

that the gate-enhanced PEC performance is sustained during prolonged operation rather than being a transient effect. To further quantify the effect of gate bias on photocarrier separation, the charge-separation efficiency was evaluated as a function of applied potential under different gate voltages. As shown in Figure 5E, charge-separation efficiency improves with increasing gate voltage, reaching over 30% at Vgs = 7 V—2.4 times higher than that without bias. This indicates that the applied gate bias establishes a vertical electric field across the photoanode, facilitating the separation of photogenerated electron-hole pairs and suppressing bulk and interfacial recombination. Reverse gate bias results (Figure 5F, with a sacrificial agent) show a stepwise decline in photocurrent, attributed to the formation of an internal reverse electric field that inhibits carrier separation and promotes recombination.

To confirm the universality of this modulation strategy, VFEPA devices with TiO_2, WO_3, Fe_2O_3, and $BiVO_4$ photoanodes were tested (Figure S21). All exhibited a similar gate-tunable enhancement in photocurrent, demonstrating the broad applicability of this field-effect-assisted design across various PEC systems.

Gate-induced charge separation and transport mechanism

To clarify how gate bias improves the PEC response, we examined the charge transfer, recombination, leakage current, spectral response, and photovoltage behavior of the VFEPA device. Photoelectrochemical impedance spectroscopy (PEIS) spectra (Figure 6A) show that the arc radius decreases with increasing Vgs, reflecting lower charge transfer resistance and improved separation. Building on this, the Bode plot (Figure 6B) reveals that as gate voltage increases, the overall phase in the high-frequency region increases, indicating enhanced capacitive behavior of the device. This helps suppress carrier recombination and improves the separation efficiency of photocarriers. Meanwhile, the noticeable left shift of the peak frequency (f_{max}) in the Bode plot indicates a prolonged carrier lifetime τ ($\tau \approx 1/2\pi f_{peak}$). Consistent with the PEIS results, Mott-Schottky analysis (Figure S22; Table S2) confirms gate-induced modulation of the interfacial electronic structure. The positive slopes of all curves verify the n-type character of ZnO, while the reduced slope and shifted flat-band potential with increasing gate voltage indicate an increased apparent donor density (from 8.569×10^{19} to 27.787×10^{19} cm^{-3}) and modified interfacial band bending. This is in good agreement with the simulated gate-induced potential redistribution and further supports enhanced carrier separation and transport under gate bias. Photoluminescence (PL) response spectra (Figure 6C) show a gradual decrease in emission intensity with increasing gate voltage. The main peak at ~450 nm corresponds to the characteristic recombination emission of the ZnO active layer, indicating suppressed radiative recombination and prolonged photocarrier lifetime.

Another critical issue to be addressed is the additional power consumption induced by gate control, which largely depends on the gate leakage current (I_{gl}). As shown in Figure 6D, the magnitude of I_{gl} is approximately 10^{-6} mA/cm^2, much lower than the photocurrent density of VFEPA (0.85 mA/cm^2). This indicates that the electrical energy (Vgs × I_{gl} × t) consumed by gate modulation is negligible in magnitude compared with both the incident

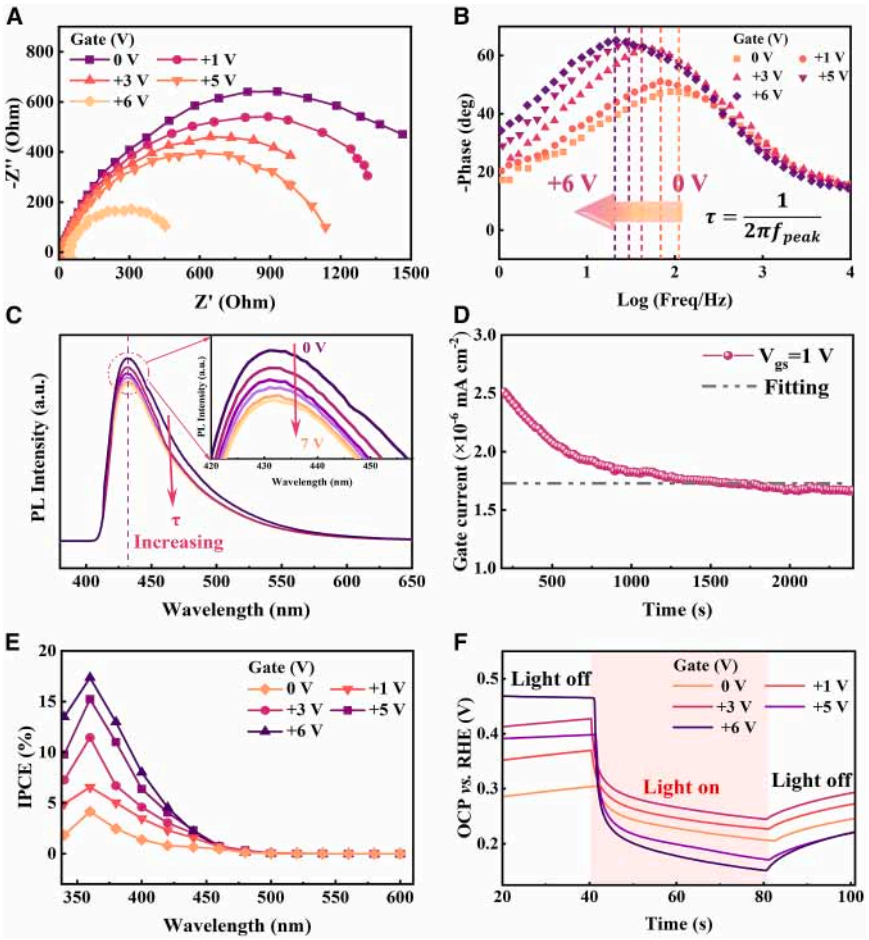


Figure 6. Mechanistic evidence for gate-enhanced charge separation and transport

(A) Photoelectrochemical impedance spectroscopy (PEIS) of the VFEPA device under different gate voltages.

(B) Bode plot of the VFEPA device under different gate voltages.

(C) Photoluminescence (PL) spectroscopy response plots of the VFEPA device under different gate voltages.

(D) Gate leakage current characteristics; specifically, a gate leakage current (I_{gl}) was obtained under electrolyte conditions by applying the gate bias Vgs between the gate and source terminals while directly recording the output current, and the measured current was normalized by the effective device area (2 × 2 cm^2).

(E) Incident photon-to-current efficiency (IPCE) spectra of the VFEPA device under different gate voltages.

(F) Open-circuit potential (OCP) curves of the VFEPA measured under chopped illumination at different gate voltages.

optical power and the output electrical/chemical energy of the device.

Figures 6E and S23 present the incident photon-to-current efficiency (IPCE) and absorbed photon-to-current efficiency (APCE) spectra of the VFEPA device under different gate voltages. Both exhibit pronounced peaks in the 350–450 nm range, corresponding to the strong UV absorption of ZnO. As Vgs increases, IPCE and APCE values rise markedly. At Vgs = 6 V, the IPCE peak reaches 17.5% (4.2 times higher than without gate voltage), while the APCE exceeds 50.8%. It should be noted that the main optical absorption edge of ZnO appears near 400 nm in the UV-vis spectrum, and the IPCE/APCE response edge extends to ~450 nm. This extended response edge is attributed to weak sub-band-gap (or band-tail) absorption associated with defects, local disorder, and grain-boundary-related states in the ZnO film, together with the enhanced separation and extraction of these weakly excited carriers under the gate electric field rather than to a true red shift of the intrinsic absorption edge.

Furthermore, the open-circuit potential (OCP) was evaluated from the OCP curves under different gate voltages (Figures 6F and S24), with $\Delta V_{OC} = |OCP_{light} - OCP_{dark}|$, and the corresponding values are summarized in Table S3. The ΔV_{OC} of the VFEPA increases markedly with gate voltage, rising from 0.100 to 0.314 V vs. reversible hydrogen electrode (RHE). This trend indicates that the gate field enhances the photovoltage response of the photoanode and increases the extent of interfacial band-bending modulation under illumination. The larger charge in OCP value further suggests that, under positive gate bias, photogenerated electron-hole pairs are separated more efficiently, while interfacial/surface recombination is more effectively suppressed.

To further demonstrate the practical relevance of the ZnO-based VFEPA strategy, we evaluated its application in PEC H_2O_2 production as a representative solar-to-chemical conversion process. The results show that gate-voltage modulation enhances H_2O_2 generation, consistent with the improved photocarrier separation and transport discussed above. The detailed experimental data, quantitative analysis, and related discussion are provided in Note S3 and Figures S25–S27.

Conclusion and outlook

This study presents a high-performance VFEPA by integrating photoelectrode materials with a FET structure. Unlike other approaches focused on material design or band engineering, we introduce gate-field modulation as a dynamic and effective strategy to enhance PEC performance. The gate-induced electric field promotes efficient photocarrier separation and directional transport, suppresses recombination, and extends carrier lifetime—enabled by the gate-induced vertical electric field across the nanometer-scale channel. Gate bias also enables precise tuning of band bending in the ZnO layer, reducing both the Al/ZnO Schottky barrier and the interfacial potential at the ZnO/electrolyte junction. This facilitates electron extraction and optimizes charge collection. At Vgs = 6 V, the H_2O_2 production rate reached 48 μmol L^{-1} h^{-1}, 1.6 times higher than the pristine ZnO

film. The IPCE increased from 4.2% to 17.5%, and the additional energy consumption from the gate field was negligible. Moreover, this modulation strategy is applicable to other photoelectrode materials beyond ZnO film, indicating broad versatility.

Looking forward, several challenges should be addressed to further advance gate-field-modulated photoanodes toward practical solar fuel production. The device architecture needs to be extended beyond model ZnO systems to broader semiconductor photoelectrodes with stronger visible-light absorption and higher catalytic activity. The stability of the gate dielectric and electrode under long-term illumination, bias, and electrolyte exposure must be carefully optimized because leakage current, dielectric degradation, or interfacial corrosion could limit device durability. The geometry and thickness of the photoactive layer, dielectric layer, and current-collecting electrode should be rationally designed to maximize field penetration while maintaining efficient light absorption and charge extraction. In addition, scalable fabrication strategies will be needed to translate this device-level concept from small-area proof-of-concept electrodes to larger PEC systems. Future studies should also clarify how gate-field modulation affects reaction selectivity, product formation, and energy balance under realistic operating conditions. Addressing these issues will help establish electrostatic field modulation as a general strategy for improving solar-driven chemical conversion.

METHODS

Chemical reagents and materials

All chemical reagents and chemicals used in this study, including acetone, ethanol, and KOH, were purchased from Aladdin Reagent (China). The magnetron sputtering targets, including Al, Fe, W, Ti, Bi, and V; Cu targets; and ZnO ceramic targets were supplied by Beijing Zhongnuo New Material Technology (China). The oxygen and argon gases required for magnetron sputtering were obtained from Lanzhou Yongfang Gas (China). The p-type heavily doped silicon wafers (with a 300 nm silicon oxide layer) were purchased from Sujing Electronics Technology Material (China). The commercial crack colloidal solution was supplied by Guangzhou Minnie Cosmetics (China), and the AB adhesive was obtained from Shenzhen Jinsibond Adhesive (China). Distilled water was used for all preparation processes, and all chemical reagents were of analytical grade.

Preparation of the VFEPA device

First, the p-type silicon wafers were sequentially immersed in anhydrous ethanol and acetone and ultrasonically treated for 20 min in each solution to remove surface impurities and organic residues. The wafers were then dried with nitrogen gas and further cleaned using a plasma cleaner to enhance surface energy. Oxygen plasma was used at a cleaning power of 40 W and a duration of 10 min. After cleaning, the edges of the wafers were sealed with high-temperature-resistant tape. The commercial acrylic emulsion was dispersed in a diluent (0.2–3 g/mL) and ultrasonically filtered for 30 min. The solution was then filtered using a Whatman filter (1 mm) and left in a sealed bottle overnight. The extracted suspension was drop cast onto the surface of the silicon wafers, followed by spin coating at 1,500 rpm for 20 s. The spin-coated wafers were dried on a heating stage at 60°C, where a uniform and continuous crack network pattern formed spontaneously. The wafers were then placed in a direct current (DC) sputtering chamber, and sputtering commenced when the chamber pressure was reduced to below 1×10^{-4} Pa. Argon was used as the working gas with a flow rate of 12 sccm, a working pressure of 0.73 Pa, a sputtering power of 30 W, and a sputtering time of 30 min. The samples were subsequently immersed in a mixed solution of acetone and KOH (acetone:KOH solution = 3:1) and ultrasonically treated to remove the sacrificial acrylic emulsion layer, yielding a uniform and continuous Al mesh electrode.

A ZnO thin film was deposited on the Al mesh electrode using radio-frequency (RF) sputtering. Sputtering commenced when the vacuum level reached below 1×10^{-4} Pa. The initial chamber pressure was adjusted to 2.7 Pa, and RF power at 50 W was used to generate a plasma glow. The substrate temperature was 300°C. The working pressure was then adjusted to 1.5 Pa, with a sputtering power of 150 W. During sputtering, the argon-to-oxygen gas ratio was maintained at 95:5, and the sputtering duration was 1.5 h. After RF sputtering, the samples were placed in a muffle furnace for annealing at 350°C for 2 h. A metal contact electrode was prepared by covering the device surface with a mask. A layer of Ag was sputtered onto the Al mesh electrode using DC sputtering to serve as the back electrode. The oxide layer at the bottom of the silicon wafer was removed, and Cu was sputtered onto the P++ silicon surface as the contact electrode. Finally, the high-temperature-resistant tape was removed, and the bottom silicon wafer and the edges of the active layer films were encapsulated with AB adhesive. Finally, the VFEPA device was obtained. The remaining active layer materials were also prepared by reactive sputtering. The TiO_2 thin film was fabricated through reactive sputtering with a working pressure of 1.0 Pa. The substrate temperature was 300°C. Argon was used as the working gas at a flow rate of 28 sccm, while oxygen was used as the reactive gas at a flow rate of 9 sccm. The sputtering power was set at 130 W. After sputtering, the film was annealed in a muffle furnace at 450°C for 2 h. The WO_3 thin film was also prepared via reactive sputtering at a working pressure of 3.4 Pa, and the substrate temperature was 300°C. The argon-to-oxygen flow ratio was 3:2. The final device was annealed in a muffle furnace at 450°C for 2 h. The α-Fe_2O_3 thin film was prepared by reactive sputtering, with a 2-mm-thick Fe target placed in a strong magnetic target position. The substrate temperature was 350°C, the working pressure was 0.5 Pa, and the argon-to-oxygen flow ratio was 4:3. The sputtering power was set at 120 W. After sputtering, the samples were annealed in a muffle furnace at 500°C for 2 h. The $BiVO_4$ thin film was prepared through reactive co-sputtering. The Bi and V targets were placed in two target positions, and the cooling water temperature was maintained below 12°C. During sputtering, the argon-to-oxygen flow ratio was 3:1, with a total working pressure of 1.5 Pa. The Bi target sputtering power was 20 W, and the Bi/V power ratio was approximately 1:1.2 to maintain a stoichiometric Bi:V ratio of 1:1. The substrate temperature was 350°C. After sputtering, the films were annealed at 500°C for 1 h.

Sample characterization

The overall morphology of the VFEPA was observed using a field-emission scanning electron microscope (Thermo Fisher

Scientific, Apreo S, USA). The element distribution in the device was analyzed using EDS (Bruker XFlash 6 | 60 Silicon Drift Detector [SDD]) supported by SEM. TEM (FEI Tecnai F30, the Netherlands) was used to characterize the microstructure of the ZnO active layer. HRTEM and HAADF imaging coupled with EDS mapping (Bruker XFlash 6 | 60 SDD) were further employed to examine the lattice structure and elemental distribution. A high-resolution optical microscope (3D measuring laser microscope, OLS5100) was used to observe the morphology of the Al mesh electrode. The crystal structure of the ZnO film was characterized using XRD (X'pert pro-X-ray) with Cu Kα radiation. Raman scattering was performed with a 550 nm laser source on the HORIBA IHR 550 laser confocal Raman spectrometer. XPS (Kratos AXIS Ultra DLD) was employed to analyze the chemical state of the device and identify its constituent elements. The optical absorption, transmission, and reflection characteristics of the ZnO thin film over the wavelength range of 300–800 nm were tested and characterized using a UV-vis spectrophotometer (Hitachi Corporation U-3900H). An electrostatic force microscope (Bruker Dimension Icon) was used to analyze the distribution of electrostatic forces on the device surface and the gate electric field distribution on the Al mesh electrode under different gate voltages. An atomic force microscope (tapping mode, Bruker Dimension Icon) was used to measure the surface morphology and depth profile of the ZnO active layer. A Kelvin probe force microscope (Bruker Dimension Icon) was utilized to analyze the V_{CPD} and SPV distribution on the device surface at different gate voltages. TUNA (Bruker Dimension Icon) was employed to measure and analyze the nanoscale distribution of photocurrent on the device surface under different gate voltages. PL spectroscopy (OmniPL, Zolix Instruments) was used to indirectly analyze the recombination and luminescence of carriers within the photoanode under different gate biases. The gate electric field and photocarrier distributions of the VFEPA device were simulated using the COMSOL Multiphysics semiconductor module. The incident light intensity at each fixed wavelength was measured with a power meter (Coherent, LabMax TOP), which ensured accurate calibration of the monochromatic light power for IPCE measurements. The PEC performance of the VFEPA was tested using an electrochemical workstation (Solartron Analytical, Energylab XM, UK) in combination with a probe station testing system (GP200-8, Nanjing Xince Software Technology). The current-voltage (I-V) characteristics of the device during bending were measured using a Keithley 2400 source meter.

PEC performance

PEC tests (Solartron Analytical, Energylab XM) were conducted by dropping the electrolyte onto the surface of the VFEPA device using a standard three-electrode probe system. The VFEPA device was used as the WE, the Ag/AgCl electrode as the RE, and the platinum wire electrode as the CE. The electrolyte used for the tests was a mixed sulfate solution (pH = 7, 25°C) with Na_2SO_3 (0.1 M) as a hole scavenger. Simulated AM 1.5 G solar illumination was provided by a high-voltage Xe lamp (500 W) with a UV filter and a light intensity of 100 mW/cm^2. Linear sweep voltammetry (LSV) was used to measure the J-V curve of the VFEPA device, with a voltage scan range from −0.3 to 0.6 V (vs. Ag/AgCl) and a scan rate of 10 mV/s. The constant-potential polarization mode was used to test the photoresponse curves of the VFEPA device under different gate voltages, with a polarization potential of 0.4 V (vs. Ag/AgCl). PEIS was performed under simulated solar illumination and a constant potential of 0.4 V (vs. Ag/AgCl). The carrier-separation efficiency of the VFEPA device under different gate voltages was calculated by the ratio of the measured photocurrent density to the theoretical maximum photocurrent density. The injection efficiency of the VFEPA device was obtained by comparing the photocurrent density in the absence of a hole scavenger with that in the presence of a hole scavenger. The IPCE was measured at a constant potential of 0.8 V (vs. Ag/AgCl), and the APCE was calculated by dividing the IPCE by the film absorbance. All potentials mentioned here were converted to the RHE scale.

PEC synthesis of H_2O_2

The production of H_2O_2 was carried out in a specially designed dual-layer, dual-chamber reaction cell. A Nafion membrane (N117) was used as a proton-exchange membrane to separate the VFEPA from the platinum sheet electrode, which served as the cathode. The Ag/AgCl RE was placed at one end of the photoanode. A 0.5 M $KHCO_3$ aqueous solution (pH = 7.1) was used as the electrolyte, and the electrolyte was continuously purged with high-purity argon gas (≥99.999%) through a glass gas-dispersion tube for 30 min. During the purging process, the argon gas flow rate was adjusted to a moderate level to ensure efficient removal of dissolved oxygen while avoiding excessive disturbance of the electrolyte. Cooling water was circulated through the entire dual-chamber cell to maintain the electrolyte temperature at 4°C, preventing thermal decomposition of H_2O_2. A 500 W Xe lamp (AM 1.5 G, 100 mW/cm^2) was used as the light source, positioned 3 cm from the reaction solution. The reaction was carried out using an electrochemical workstation (Solartron Analytical, Energylab XM) at a constant potential of 0.8 V (vs. Ag/AgCl) and simulated sunlight illumination (AM 1.5 G, 100 mW/cm^2). The amount of H_2O_2 produced was determined by the iodometric method. Typically, 1 mL of 0.1 M potassium hydrogen phthalate ($C_8H_5KO_4$) aqueous solution and 0.4 M KI aqueous solution were simultaneously added to 2 mL of the reaction solution and stirred vigorously for 2 min. H_2O_2 reacted with I^- to produce I_3^-, and the production of H_2O_2 was evaluated through UV-vis absorption measurements at 351 nm.

RESOURCE AVAILABILITY

Lead contact

Requests for further information and resources should be directed to and will be fulfilled by the lead contact, Di Wei (weidi@binn.cas.cn).

Materials availability

The materials generated in this study are available from the lead contact upon reasonable request.

Data and code availability

All data and source code underlying this study are available from the corresponding author upon reasonable request.

ACKNOWLEDGMENTS

This work was supported by the China Postdoctoral Science Foundation (certificate no. 2025M781041) and the National Natural Science Foundation (grant no. 22479016). The authors thank their colleagues in the research group for valuable discussions and technical support throughout the project. Special thanks to the technicians from the School of Physical Science and Technology for their assistance with experimental setups and data analysis. This work was supported by the Supercomputing Center of Lanzhou University.

AUTHOR CONTRIBUTIONS

W.H. conceived and supervised the project. X.W., D.W., and W.H. proposed the experimental concept and methodology. X.W. and T.H. contributed to the experimental methods. Y.X. and Y.P. conducted the FEA calculations. X.W. and Y.P. performed the atomic force microscope photoconductive module measurements. X.W. carried out the main experiments, data analysis, and visualization. X.W. wrote the original draft. D.W., W.H., and X.L. reviewed and edited the manuscript. W.H. provided the experimental equipment and corresponding financial support. All authors have given approval to the final version of the manuscript.

DECLARATION OF INTERESTS

The authors declare no competing interests.

SUPPLEMENTAL INFORMATION

Supplemental information can be found online at https://doi.org/10.1016/j.device.2026.101185.

Received: February 2, 2026
Revised: March 24, 2026
Accepted: May 11, 2026
Published: June 2, 2026

REFERENCES

1. Wang, Q., and Domen, K. (2020). Particulate Photocatalysts for Light-Driven Water Splitting: Mechanisms, Challenges, and Design Strategies. Chem. Rev. *120*, 919–985. https://doi.org/10.1021/acs.chemrev.9b00201.
2. Mamun, A.A., Chowdhury, A.H., Billah, A., Karim, J., Hussain, A.O., Rahman, F., and Talukder, M.A. (2025). Advancing Transition Metal Oxide Photoelectrodes for Efficient Solar-Driven Hydrogen Generation: Strategies and Insights. Adv. Energy Mater. *15*, 2501766. https://doi.org/10.1002/aenm.202501766.
3. Xia, C., Wang, H., Kim, J.K., and Wang, J. (2021). Rational Design of Metal Oxide-Based Heterostructure for Efficient Photocatalytic and Photoelectrochemical Systems. Adv. Funct. Mater. *31*, 2008247. https://doi.org/10.1002/adfm.202008247.
4. Liu, G., Ma, G., Mu, H., Li, J., Li, F., Zhu, M., and Zhang, J. (2025). Enhanced photoelectrocatalytic CO_2 reduction to CO via structure-induced carrier separation in coral-like $CuBi_2O_4$-Bi_2O_3. Sep. Purif. Technol. *358*, 130319. https://doi.org/10.1016/j.seppur.2024.130319.
5. Dabodiya, T.S., George, T., Mathew, F.A., and Vadivel Murugan, A. (2024). Ultrastable, high photoelectrocatalytic performance of altervalent cation-doped $BiVO_4$ photoanode and effect of interfacial contact with nanoporous carbon for seawater splitting using a 3D-printed flow device. ACS Appl. Energy Mater. *7*, 2309–2328. https://doi.org/10.1021/acsaem.3c03068.
6. Li, Q., Wang, Z., Li, Y., and Zhang, H. (2025). Degradation of tetracycline hydrochloride through g-C_3N_4/TiO_2 nanotube arrays for photoelectrocatalytic activation of PMS system: performance and mechanistic analysis. Mater. Sci. Semicond. Process. *185*, 108879. https://doi.org/10.1016/j.mssp.2024.108879.
7. Jia, P., Yu, Y., Chen, T., and Huang, H. (2025). "Electricity"-Assisted Catalytic Solar-to-Fuel Processes. Angew. Chem. Int. Ed. *64*, e202508809. https://doi.org/10.1002/anie.202508809.
8. Song, K., Liu, H., Chen, B., Gong, C., Ding, J., Wang, T., Liu, E., Ma, L., Zhao, N., and He, F. (2024). Toward efficient utilization of photogenerated charge carriers in photoelectrochemical systems: engineering strategies from the atomic level to configuration. Chem. Rev. *124*, 13660–13680. https://doi.org/10.1021/acs.chemrev.4c00382.
9. Wang, J., Liao, W., Tan, Y., Henrotte, O., Kang, Y., Liu, K., Fu, J., Lin, Z., Chai, L., Cortes, E., and Liu, M. (2025). Transfer dynamics of photo-generated carriers in catalysis. Chem. Soc. Rev. *54*, 6553–6596. https://doi.org/10.1039/D5CS00512D.
10. Ma, M., Wang, R., Shi, L., Li, R., Huang, J., Li, Z., Li, P., Konysheva, E.Y., Li, Y., Liu, G., and Xu, X. (2024). Defect-Expedited Photocarrier Separation in $Zn_2In_2S_5$ for High-Efficiency Photocatalytic C—C Coupling Synchronized with H_2 Liberation from Benzyl Alcohol. Adv. Funct. Mater. *34*, 2405922. https://doi.org/10.1002/adfm.202405922.
11. Shao, J., Liu, H., Jiang, X., Wang, Y., Luo, L., Li, Y., Zhang, Z., and Lu, B. (2024). High Performance Ferroelectric-modulated Photoelectrodes by Using Grid Charge Collector. Adv. Funct. Mater. *34*, 2316409. https://doi.org/10.1002/adfm.202316409.
12. Xiao, Y., Fu, J., Pihosh, Y., Karmakar, K., Zhang, B., Domen, K., and Li, Y. (2025). Interface engineering for photoelectrochemical oxygen evolution reaction. Chem. Soc. Rev. *54*, 1268–1317. https://doi.org/10.1039/D4CS00309H.
13. Park, S., Seo, D., Hong, S., Kim, G., Han, Y., Park, I., Lee, S., Park, M.J., Nam, K.M., and Um, H.D. (2025). Strategic Spatial Segregation in Silicon Photoelectrodes: Decoupling Catalytic and Optical Functions for High-Efficiency Solar Water Splitting. Small Struct. *6*, 2400644. https://doi.org/10.1002/sstr.202400644.
14. Fang, Y., Li, M., Gao, Y., Wen, Y., and Shan, B. (2025). Static Organic p-n Junctions in Photoelectrodes for Solar Ammonia Production with 86% Internal Quantum Efficiency. Angew. Chem. Int. Ed. *64*, e202415729. https://doi.org/10.1002/anie.202415729.
15. Peng, P., Wang, Z., and Wei, D. (2026). Modulating multi-ion dynamics for high-performance iontronic systems. Iontronics *2*, 5. https://doi.org/10.20517/iontronics.2026.05.
16. Zhao, F., He, Y., Li, X., Yang, K., Chen, S., Jiang, Y., Wang, X.-S., Song, C., and Liu, X. (2026). Ultrafast Sulfur Redox Dynamics Enabled by a PPy@N-TiO_2 Z-Scheme Heterojunction Photoelectrode for Photo-Assisted Lithium–Sulfur Batteries. Nano-Micro Lett. *18*, 92. https://doi.org/10.1007/s40820-025-01946-3.
17. Xie, H., Song, Y., Jiao, Y., Gao, L., Shi, S., Wang, C., and Hou, J. (2024). Engineering surface passivation and hole transport layer on hematite photoanodes enabling robust photoelectrocatalytic water oxidation. ACS Nano *18*, 5712–5722. https://doi.org/10.1021/acsnano.3c11638.
18. Zhi, Y., Leng, X., Wang, D., and Xu, L. (2024). Dual Modification strategy: Passivation layer and cocatalyst on hematite for improved photoelectrochemical water oxidation. ACS Appl. Mater. Interfaces *16*, 54058–54066. https://doi.org/10.1021/acsami.4c14137.
19. Jeon, T.H., Park, C., Kang, U., Moon, G.-h., Kim, W., Park, H., and Choi, W. (2024). Photoelectrochemical water oxidation using hematite modified with metal-incorporated graphitic carbon nitride film as a surface passivation and hole transfer overlayer. Appl. Catal. B Environ. Energy *340*, 123167. https://doi.org/10.1016/j.apcatb.2023.123167.
20. Wang, M., Langer, M., Altieri, R., Crisci, M., Osella, S., and Gatti, T. (2024). Two-dimensional layered heterojunctions for photoelectrocatalysis. ACS Nano *18*, 9245–9284. https://doi.org/10.1021/acsnano.3c12274.
21. Feitosa, M.H.A., Santos, A.M., Wong, A., Moraes, C.A.F., Grosseli, G.M., Nascimento, O.R., Fadini, P.S., and Moraes, F.C. (2024). Photoelectrocatalytic removal of antibiotic ciprofloxacin using a photoanode based on

Z-scheme heterojunction. Chem. Eng. J. *493*, 152291. https://doi.org/10.1016/j.cej.2024.152291.

22. Shen, W., Dong, Y., Wu, J., Lv, J., Bao, Z., Cui, J., Zhang, J., and Xu, G. (2024). Visible light-driven photoelectrocatalytic degradation of tetracycline on $NiFe_2O_4$/SiNWs heterojunction. Appl. Surf. Sci. *647*, 158880. https://doi.org/10.1016/j.apsusc.2023.158880.
23. Jayeola, K.D., Sipuka, D.S., Sebokolodi, T.I., Nkwachukwu, O.V., Muzenda, C., Koiki, B.A., Babalola, J.O., Zhou, M., and Arotiba, O.A. (2024). An S-Scheme CeO_2/Bi_2O_2S heterojunction photoanode for the photoelectrocatalytic degradation of sulfamethoxazole in synthetic and real wastewater. Electrochim. Acta *507*, 145160. https://doi.org/10.1016/j.electacta.2024.145160.
24. Wang, K., Liu, B., Liu, Z., Jiang, X., Zhang, Z., and Han, W. (2023). Improved photocarrier separation in Ga/Fe gradient $(Ga, Fe)_2O_3$ thin films. Appl. Phys. Lett. *122*, 203901. https://doi.org/10.1063/5.0143076.
25. Feng, X., Sun, T., Feng, X., Yu, H., Yang, Y., Chen, L., and Zhang, F. (2024). Single-Atomic-Site Platinum Steers Middle Hydroxyl Selective Oxidation on Amorphous/Crystalline Homojunction for Photoelectrochemical Glycerol Oxidation Coupled with Hydrogen Generation. Adv. Funct. Mater. *34*, 2316238. https://doi.org/10.1002/adfm.202316238.
26. Li, W., Lu, Y., Tang, Y., and Sun, H. (2024). Carbon–carbon triple bond-containing materials for photo (electro) catalytic solar hydrogen production. Carbon Energy *6*, e527. https://doi.org/10.1002/cey2.527.
27. El Hattab, A., Mirzaei, A., Nada, A.A., Shayegan, Z., Roualdes, S., and Chaker, M. (2025). $TiO_2/BiVO_4$ dual photoanodes: Extending light harvesting and addressing band edge misalignment for photoelectrochemical water splitting. J. Power Sources *643*, 237070. https://doi.org/10.1016/j.jpowsour.2025.237070.
28. Perumal, S., Lim, T., Marimuthu, T., and Seo, J. (2025). Electrochemical defect control of bulky crystalline $CuBi_2O_4$ film and the band edge alignment for photoelectrochemical water reduction. Appl. Surf. Sci. *679*, 161166. https://doi.org/10.1016/j.apsusc.2024.161166.
29. Zhang, Z., Chen, X., Hao, R., Feng, Q., and Xie, E. (2023). Van der Waals heterojunction modulated charge collection for H_2O_2 production photocathode. Adv. Funct. Mater. *33*, 2303391. https://doi.org/10.1002/adfm.202303391.
30. Zhang, Z., Lindley, S.A., Chen, T., Cheng, X., Xie, E., Han, W., Toma, F.M., and Cooper, J.K. (2022). Local charge transport at the interface of semiconductor and charge transport mediator. Adv. Opt. Mater. *10*, 2201247. https://doi.org/10.1002/adom.202201247.
31. Lin, Y., Yang, F., Wang, X., Zhong, L., and Yu, D. (2025). Organic Gradient Homojunction via D-A Engineering Enables Photoelectric/Photothermal Dual-Assisted Catalysis Toward Full Spectrum Light-Coupled Low-Temperature Seawater Batteries. Adv. Mater. *37*, 2415608. https://doi.org/10.1002/adma.202415608.
32. Wang, H.C., Li, H.M., Yang, T., Ji, J.W., Yue, X.Z., Liu, Q.C., Yi, S.S., and Zhu, Y. (2024). Enhanced water oxidation of hematite photoanodes via localized n-p homojunctions induced by gradient Zn^{2+} doping. Adv. Funct. Mater. *34*, 2406545. https://doi.org/10.1002/adfm.202406545.
33. Gunawan, M., Bowdler, O., Zhou, S., Fang, X., Zhang, Q., Sakamoto, Y., Sun, K., Gunawan, D., Chang, S.L.Y., Amal, R., et al. (2025). Ferroelectric Polarization-Induced Performance Enhancements in $BiFeO_3/BiVO_4$ Photoanodes for Photoelectrochemical Water Splitting. Adv. Funct. Mater. *35*, 2417651. https://doi.org/10.1002/adfm.202417651.
34. Guo, P., Jia, M., Guo, D., Ren, T., Wang, Z.L., and Zhai, J. (2025). Progress in flexoelectric effect research and related applications. SmartSys *1*, e1. https://doi.org/10.1002/sys3.1.
35. Zhang, T., Guan, X., Zhang, Z., Wang, B., Qu, J., Zeng, W., Ye, X., and Guo, L. (2024). Photothermal catalytic hydrogen production coupled with thermoelectric waste heat utilization and thermal energy storage for continuous power generation. Nano Energy *121*, 109273. https://doi.org/10.1016/j.nanoen.2024.109273.
36. Zhi, Z., Pan, C., He, Y., Tan, Y., Gu, R., Chen, T., and Cao, D. (2026). Ferroelectric-enhanced Photoelectrochemical Water Splitting: A Review of Recent Progress on the Mechanism. Small *22*, 2412794. https://doi.org/10.1002/smll.202412794.
37. Chen, M., Tian, H., Qi, L., Zhang, Y., Yang, H., Ge, S., Zhang, L., Zhang, Y., Li, L., Cui, K., and Yu, J. (2025). Photothermal-thermoelectric synergy coupling localized surface plasmon resonance for enhanced flexible photoelectrochemical sensor performance. Chem. Eng. J. *503*, 158393. https://doi.org/10.1016/j.cej.2024.158393.
38. Zhang, S., Liu, Z., Ruan, M., Guo, Z., Zhao, W., Zhao, D., Wu, X., and Chen, D. (2020). Enhanced piezoelectric-effect-assisted photoelectrochemical performance in ZnO modified with dual cocatalysts. Appl. Catal. B Environ. *262*, 118279. https://doi.org/10.1016/j.apcatb.2019.118279.
39. Ma, C., Liu, Z., Cai, Q., Han, C., and Tong, Z. (2018). ZnO photoelectrode simultaneously modified with Cu_2O and Co-Pi based on broader light absorption and efficiently photogenerated carrier separation. Inorg. Chem. Front. *5*, 2571–2578. https://doi.org/10.1039/C8QI00596F.
40. Jia, T., Ruan, M., Li, G., Michorczyk, P., Wang, C., and Liu, Z. (2026). Ca^{2+} substitution induced phase coexistence and synergistic regulation of Ti^{3+} defects to improve piezoelectric–photocatalytic water splitting performance of $BaTiO_3$. J. Mater. Chem. A *14*, 1908–1922. https://doi.org/10.1039/D5TA08280C.
41. Liu, L., Ruan, M., Wang, C., and Liu, Z. (2024). Optimization of the BiO_8 polar group of $BiVO_4$ by Cl^--embedded modification to manipulate bulk-surface carrier separation for achieving efficient Piezo-PEC water oxidation. Appl. Catal. B Environ. Energy *354*, 124117. https://doi.org/10.1016/j.apcatb.2024.124117.
42. Han, J., and Liu, Z. (2021). Optimization and modulation strategies of zinc oxide-based photoanodes for highly efficient photoelectrochemical water splitting. ACS Appl. Energy Mater. *4*, 1004–1013. https://doi.org/10.1021/acsaem.0c02985.
43. Li, X., Wang, Z.L., and Wei, D. (2025). Iontronic logic control driven by dynamic electrical double layer regulation. Iontronics *1*, 2. https://doi.org/10.20517/iontronics.2025.02.
44. Lenz, J., Seiler, A.M., Geisenhof, F.R., Winterer, F., Watanabe, K., Taniguchi, T., and Weitz, R.T. (2021). High-performance vertical organic transistors of sub-5 nm channel length. Nano Lett. *21*, 4430–4436. https://doi.org/10.1021/acs.nanolett.1c01144.
45. Nawaz, A., Merces, L., De Andrade, D.M., de Camargo, D.H.S., and Bof Bufon, C.C. (2020). Edge-driven nanomembrane-based vertical organic transistors showing a multi-sensing capability. Nat. Commun. *11*, 841. https://doi.org/10.1038/s41467-020-14661-x.
46. Qiao, K., Dai, T., and Zou, T. (2024). A design strategy for high-performance vertical organic field-effect transistors based on reduced graphene oxide electrodes. J. Mater. Chem. C *12*, 7513–7519. https://doi.org/10.1039/D4TC01699H.
47. Harika, P., Kondavitee, G.S., Karumuri, S.R., and Lay-Ekuakille, A. (2024). High sensitivity of dielectrically modulated tunnel field effect transistor for biosensor applications. IEEE Trans. Nanobiosci. *24*, 25–36. https://doi.org/10.1109/TNB.2024.3386586.
48. Ho, S., Park, J., So, F., and Yu, H. (2025). Micropatterned Indium–Tin Oxide Grid Electrode for Vertical, Optoelectronic Field-Effect Transistors. ACS Appl. Electron. Mater. *7*, 919–924. https://doi.org/10.1021/acsaelm.4c02172.
49. Zhang, R., Yin, P.-G., Wang, N., and Guo, L. (2009). Photoluminescence and Raman scattering of ZnO nanorods. Solid State Sci. *11*, 865–869. https://doi.org/10.1016/j.solidstatesciences.2008.10.016.
50. Zheng, Y., Xu, Z., Shi, K., Li, J., Fang, X., Jiang, Z., and Chu, X. (2024). A high-performance WS_2/ZnO QD heterojunction photodetector with charge and energy transfer. J. Mater. Chem. C *12*, 18291–18299. https://doi.org/10.1039/D4TC03659J.